Modeling and Analysis of Tendon-driven Continuum Robots for Rod-based Locking

Priyanka Rao[1,4], *Student Member, IEEE,* Chloe Pogue[1,2,4], *Student Member, IEEE,*
Quentin Peyron[1,3], *Member, IEEE*, Eric Diller[2,4], *Senior Member, IEEE,*
and Jessica Burgner-Kahrs[1,4], *Senior Member, IEEE*

Abstract—**Various design modifications have been proposed for tendon-driven continuum robots to improve their stiffness and workspace. One of them is using locking mechanisms to constrain the lengths of rods or passive backbones along the robot. However, physics-based models used to predict these robots' behaviour commonly assume that the curvature of the locked portion does not change during robot actuation or that the effects of friction and gravity are negligible. In addition, these models do not consider the variations in twist on force application. In this letter, we propose a 3D static model for tendon-driven continuum robots experiencing locking due to length constraints on rods along their backbone. The proposed model is evaluated on prototypes of length 240 mm, with up to three locking mechanisms and has an accuracy of 3.63% w.r.t. length. Using the proposed model, a compliance analysis is performed studying the evolution of the robot compliance with the position of the locking mechanisms. An actuation strategy is proposed that can allow the robot to achieve the same shape with different compliance.**

Index Terms—**Modeling, Control, and Learning for Soft Robots, Flexible Robotics, Kinematics.**

I. INTRODUCTION

TYPICAL tendon-driven continuum robots (TDCRs) are faced with two major issues due to being compliant and under-actuated: (1) they may lack the stiffness required to perform tasks requiring large force transmissions at their tip and (2) they cannot easily achieve multiple curvatures as they are underactuated, and have limited controllable degrees of freedom.

There have been various approaches to improve the robot stiffness, like granular [1], scale [2], and layer jamming [3], [4]. Stiffening by controlling tendon [5] and pneumatic actuators [6] is another example, where higher tension or pressure is applied on all actuators to increase stiffness. A curvature restraining rod has also been proposed [7] that can be

[1] Continuum Robotics Laboratory, Department of Mathematical & Computational Sciences, University of Toronto, Mississauga, ON, Canada. `priyankaprakash.rao@mail.utoronto.ca`

[2] Microrobotics Lab, Department of Mechanical and Industrial Engineering, University of Toronto, `chloe.pogue@mail.utoronto.ca`

[3] DEFROST Team, INRIA Lille-Nord Europe and CRIStAL UMR CNRS 9189, University of Lille, Villeneuve d'Ascq, France.

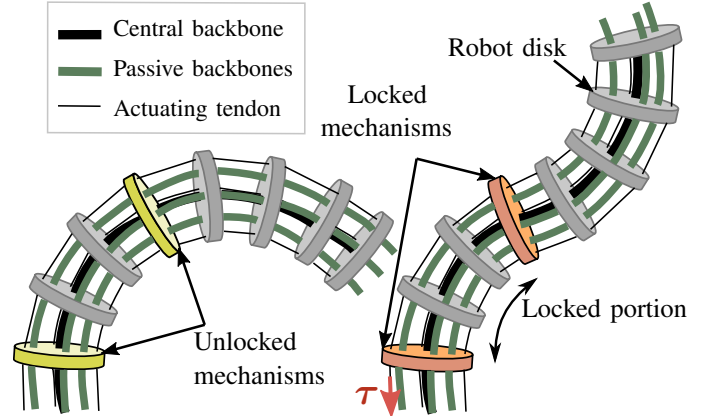[4] Robotics Institute, University of Toronto, Toronto, ON, Canada.

Fig. 1. Sequence of locking motion shown, with the multiple curvatures

inserted and retracted to vary the robot stiffness. Increasing the controllable degrees of freedom is generally achieved either by adding additional segments or by introducing length extension and retraction in a segment. Varying the tendon routing along the backbone [8]–[10] has been shown to change continuum robots' curvature and stiffness properties. Another approach to enable multiple curvatures is by changing the robot stiffness by introducing high friction material [11] to limit the motion between two sliding backbones in a tip-growing robot.

A promising approach to improving the stiffness while adding additional degrees of freedom in the literature is to use the principle of locking. Locking limits backbone motion as it prevents relative motion between some of the robot components using friction or mechanical principles. The working principle involves having these mechanisms along the robot, clutching or latching on to passive backbone elements, constraining portions of their length. These length constraints result in increased stiffness, and enable multiple curvatures along the backbone and corresponding increase in its degrees of freedom. Compared to the previous methods, locking mechanisms have the advantage of being modular and compact, as they are relatively smaller compared to the robot itself. They can be designed at the millimeter scale, with central channels to pass cables and tools.

A general TDCR design with locking mechanisms that clutch on to additional passive backbones is shown in Fig. 1. These passive backbones run parallel to the primary backbone, with tendons used to actuate the backbone itself. When two locking mechanisms are actuated, the length of the portion
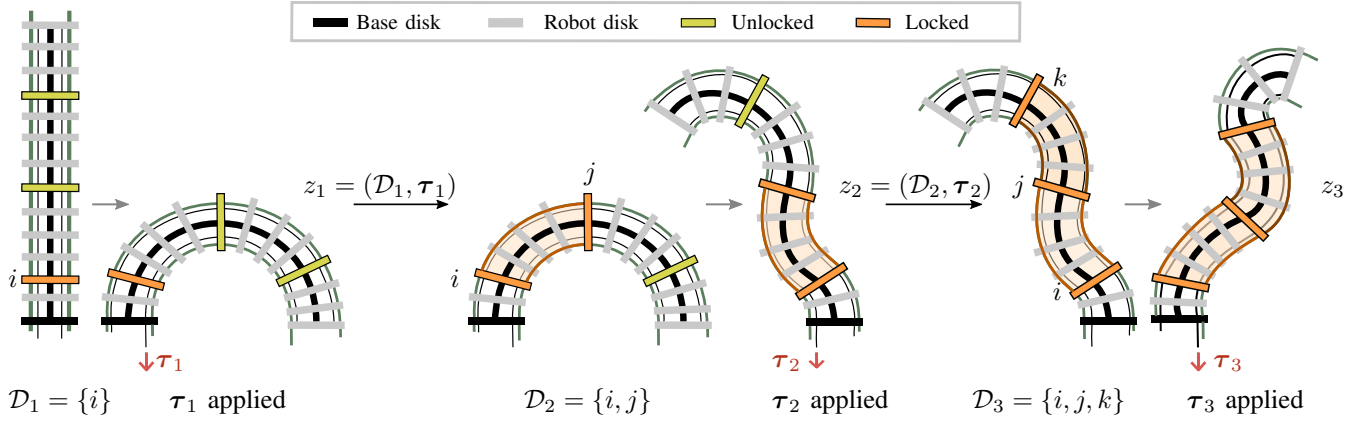
Fig. 2. Sequence of locking motion shown, for $m = 3$ for a planar case. The notation $\mathcal{D}_e$ denotes the indices of disks whose locking mechanisms are engaged and in locked state while z_e denotes the state after a tension $\boldsymbol{\tau}_e$ is applied. Starting straight configuration with disk i locked, the robot bent on application of $\boldsymbol{\tau}_1$ resulting in state $z_1 = (\mathcal{D}_1, \boldsymbol{\tau}_1)$. Disk j is then locked as well, constraining the backbones. Tension $\boldsymbol{\tau}_2$ results in z_2 and the state $z_2 = (\mathcal{D}_2, \boldsymbol{\tau}_2)$. Next, disk k is locked as well and $\boldsymbol{\tau}_3$ applied, resulting in $z_3 = (\mathcal{D}_3, \boldsymbol{\tau}_3)$.

of the passive backbones between the two mechanisms is constrained. This length-constraint increases the stiffness of the locked portion while allowing the rest of the robot to bend according to tendon actuation.

The locking mechanisms themselves can use a variety of actuation methods. For example, shape-memory alloys (SMAs) have been used to actuate these locking mechanisms to clutch on to rods [12] and cables [13]. Similarly, in our prior work [14], a magnetically-actuated mechanical lock was proposed to clutch on to passive backbones along the robot. In an alternative application, these locking mechanisms have been used to create interlaced robots that can achieve follow-the-leader deployment. Piezoelectric [15] and parallel-link mechanisms [16] in a robot have been used to clutch on to rods and retain the robot's shape, while another interlaced concentric robot follows the shape.

Modeling the impact of length-based constraints on the robot behaviour is an essential step towards formulating TDCR design, control, and motion planning paradigms. However, existing models typically assume that the segment bends as a constant curvature (CC) arc, which entails certain limiting assumptions. For example, the model proposed by Bishop et al. [13] assumes that the backbone curvature does not vary once locked. Wang et al. [17] account for this variation by considering moment coupling between the locked and unlocked portion. Additionally, both these approaches assume that the effect of frictional and gravitational forces is negligible to keep the CC assumption valid. A static model is proposed by Yang et al. [12] that accounts for these forces by assuming a piecewise-constant curvature (PCC) model, where the backbone is represented as a series of constant curvature arcs. However, all the above models assume that the twist in the backbone is negligible and do not account for 3D deformations due to external forces.

In addition to a general static model that can model 3D deformations, there is a need to study the variation in robot properties due to the introduction of locking mechanisms. In particular, there has been no study evaluating the stiffness variation of TDCRs based on the position of these locking mechanisms. Furthermore, most works restrict their study to enabling two curvatures in a single segment.

In this letter, we propose a length constraint approach to model the locked behaviour of these robots. The locked robot portion is modeled by assuming that the length constraints result in an additional internal moment that varies based on the forces acting on the robot. We implement this constraint by using the PCC assumption to model the backbone. The contributions of our letter are as follows. First, we propose a general 3D static model for TDCRs that takes into account the length constraints of locked portions, along with backbone twist, frictional, and gravitational forces. Second, we present a compliance analysis for these locking mechanisms to study the influence of locking mechanism placement on the robot's stiffness. Finally, we propose an actuation strategy using three or more locking mechanisms that can be used to achieve the same shape, but with different stiffness properties.

II. WORKING PRINCIPLE

To model the behaviour of a TDCR experiencing locking, we consider a single segment TDCR actuated by three tendons, routed through n disks with a radius of r_d placed equidistantly along the central backbone. Three passive backbones are assumed to be at a distance of r_{bb} to the central backbone in all configurations, also arranged equidistant w.r.t each other. The tendons can have different tensions applied to them which result in different shapes. We illustrate an example TDCR in Fig. 2 as we explain the working principle in the following.

In order to lock any portion of the robot, there needs to be a minimum of two locking mechanisms on the robot. If m is the number of locking mechanisms on the robot, then $m \in [2, n+1] \in \mathbb{W}$, since in addition to being placed on the n disks another could also be placed on the base disk. When two locking mechanisms at disks p and q are locked, the length of the secondary backbones between disks p and q is constrained. This locked portion has higher stiffness and can therefore, be used to obtain multiple curvatures when different tendon tensions are applied as shown in Fig. 2.

The shape of the robot depends on the sequence in which the following actions are performed: a) engaging the locking mechanisms and b) changing the tensions applied on the tendons. Let the sequence in which the above steps are performed be denoted by $\mathcal{Z} = \{z_1, z_2...z_T\}$. For any element e, $z_e = (\mathcal{D}_e, \boldsymbol{\tau}_e)$, where $\mathcal{D}_e$ denotes the set of indices of mechanisms which are locked and the vector $\boldsymbol{\tau}_e$ denotes the vector of tendon tensions applied post locking. If the notation $\text{card}(\mathcal{D}_e)$ denotes the cardinality or size of $\mathcal{D}_e$, the number of locked portions can be calculated by $d = \text{card}(\mathcal{D}_e) - 1$. If the size of $\mathcal{D}_e$ is less than 2, no portion is locked as you need at least two locking mechanisms to lock the backbones. From a design perspective, we assume that one locking mechanism is always actuated to prevent the secondary backbones from sliding off.

If mechanisms on disks i, j, and k are locked, $\mathcal{D}_e$ is denoted as $\{i, j, k\}$, where $i < j < k$, and the portions between i and j, and between j and k is locked. For example, consider the robot with $m = 3$ locking mechanisms placed at disks $\{i, j, k\}$ depicted in Fig. 2. First, mechanism at i is locked and a tension $\boldsymbol{\tau}_1$ is applied. Next, the mechanism at j is locked and a tension of $\boldsymbol{\tau}_2$ is applied. Finally, the mechanism at k is also locked and the tension $\boldsymbol{\tau}_3$ is applied.

III. ROBOT REPRESENTATION

In this section we detail the backbone parameterization using the PCC assumption. We follow the nomenclature and methods defined in [18]. We assume that the backbones do not experience elongation or shear as it is negligible compared to their bending. We consider the model of a single segment robot i.e. there is only one set of tendons actuating the robot, terminating on the last disk. The entire segment is divided further into subsegments, each subsegment j consisting of the portion of the central backbone between disks $j - 1$ and j, including the disk j.

A. Backbone kinematic representation

The point O_{j-1} describes the center of disk $j - 1$ and represents the base of subsegment j. There is a local frame of reference attached to each disk, with the x-axis of this local frame pointed towards the location of the tendon marked 1, and the local z-axis tangent to the backbone. The tendons and passive backbones are numbered in an anti-clockwise manner as shown in Fig. 3. The segment of length l is divided equally between the n subsegments, each of length $l_j = l/n$.

We assume that the portion of the backbone in each subsegment bends as a circular arc, following the piece-wise constant-curvature assumption [19], [20]. The configuration parameters of the entire segment can then be represented by the parameters, $\mathbf{X}_{\mu,j} = [\kappa_{x,j}, \kappa_{y,j}, \epsilon_j]^T$ for $j = 1, 2..n$, where $\kappa_{x,j}$ and $\kappa_{y,j}$ represent the components of bending curvature along the x and y axis, and ϵ_j represents the torsional component of curvature. Therefore, $3n$ parameters
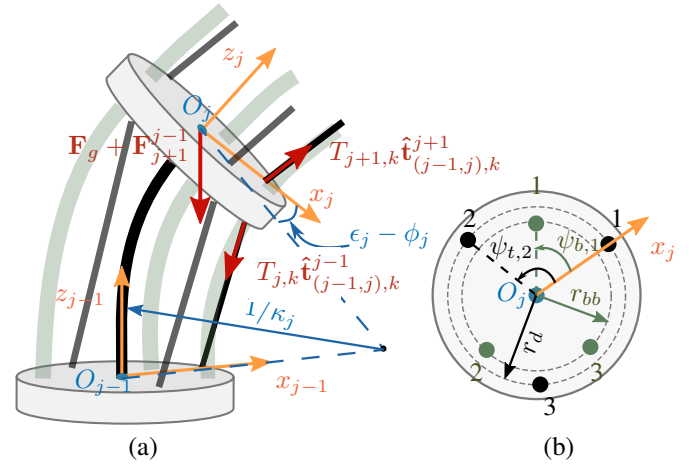

Fig. 3. (a) Diagrammatic representation of the forces acting on the robot marked in red and coordinate axes in orange. (b) Cross section of the disk showing the anti-clockwise numbering of tendons and backbones. The passive backbones are placed at a radius of r_{bb}, marked in green, while the tendons are placed at a radius of r_d, marked in black.

are required to represent the entire backbone. The resulting bending curvature, κ_j and plane of bending, ϕ_j is given by

$$\kappa_j = \sqrt{\kappa_{x,j}^2 + \kappa_{y,j}^2} \qquad (1)$$

$$\phi_j = \text{atan2}\left(\kappa_{y,j}, \kappa_{x,j}\right) \qquad (2)$$

In a subsegment j with a base at O_{j-1} and associated reference frame, the coordinates of the end-point of the backbone coincide with the center of the next disk at O_j. A point on the central backbone at an arc length of s, defined w.r.t. the frame of reference of disk $j - 1$ is given by

$$\mathbf{p}_j^{j-1}(s) = \begin{bmatrix} \frac{\cos\phi_j}{\kappa_j}\left(1 - \cos(\kappa_j s)\right) \\ \frac{\sin\phi_j}{\kappa_j}\left(1 - \cos(\kappa_j s)\right) \\ \frac{1}{\kappa_j}\sin(\kappa_j s) \end{bmatrix}. \qquad (3)$$

The transformation between reference frames $j - 1$ and j is given by

$$\mathbf{T}_j^{j-1} = \begin{bmatrix} \mathbf{R}_z(\phi_j)\mathbf{R}_y(\kappa_j l_j)\mathbf{R}_z(\epsilon_j l_j - \phi_j) & \mathbf{p}_j^{j-1}(l_j) \\ \mathbf{0} & 1 \end{bmatrix} \qquad (4)$$

where $\mathbf{R}_z$ and $\mathbf{R}_y$ represent rotations about the local z and y axis respectively. The transformation matrix between the reference frames of two subsegments is given by sequentially multiplying the corresponding transformation matrices of all disks between the frames of interest.

B. Disk constraints on tendons and passive backbones

The tendons are arranged at angles $[\psi_{t,1}, \psi_{t,2}, \psi_{t,3}]$ and the passive backbones at angles $[\psi_{b,1}, \psi_{b,2}, \psi_{b,3}]$ as shown in Fig. 3. The tendons are assumed to be partially constrained and the coordinates of tendon k intersecting at disk j, w.r.t. frame j is calculated by

$$\mathbf{p}_{t,(j,k)}^j = r_d \begin{bmatrix} \cos(\psi_{t,k}) & \sin(\psi_{t,k}) & 0 \end{bmatrix}^\top \qquad (5)$$

The coordinates of the passive backbone k can be obtained from (5) by substituting $\psi_{t,k}$ with $\psi_{b,k}$, and r_d with r_{bb}.

C. Coordinates of points along passive backbones

Since we consider that the length of the locked portion of the passive backbones, consisting of multiple subsegments, remains constant, we need to calculate their length within a subsegment. To do so while considering their experienced twist, we approximate a continuous secondary backbone by a series of w intermediate points. Since we assume that a subsegment has constant torsional curvature, the twist angle at an arc length of $s \in [0, l_j]$ in the subsegment is given by $\epsilon_j s$. Using equations (3), (4) and (5), the corresponding point lying on backbone k w.r.t. the frame $j - 1$ is given by

$$\mathbf{p}_{b,(j,k)}^{j-1}(s) = \begin{bmatrix} \mathbf{R}^{j-1}(s) & \mathbf{p}_j^{j-1}(s) \\ \mathbf{0} & 1 \end{bmatrix} \begin{bmatrix} \mathbf{p}_{b,(j,k)}^j \\ 1 \end{bmatrix} \quad (6)$$

$$\mathbf{R}^{j-1}(s) = \mathbf{R}_z(\phi_j)\mathbf{R}_y(\kappa_j s)\mathbf{R}_z(\epsilon_j s - \phi_j) \quad (7)$$

The coordinates of the w points can be obtained by equating $s = (m/w)l_j$, where $m = 1, 2...w$.

IV. STATIC MODEL

We consider a tension τ_k applied at the tendon k to actuate the robot. The static model involves finding the mapping from these applied tensions to the resulting position and orientation of the entire backbone. We assume that the tendons follow a partially constrained path, defined in [18], where the portion of the tendon between consecutive disks is considered to be a straight line. The force equilibrium equations have been adapted from the model written for a standard TDCR design, proposed in [20]. While the above methods have been used to model the unlocked robot, we introduce additional length constraints on the portion of the locked passive backbones to model the robot in the locked state. Once the force and moment equilibrium equations are written for each subsegment, the Hooke's law is used to find the resulting constitutive equations. The backbone is assumed to be inextensible, and its weight negligible compared to the weight of the disks.

A. Forces and moments

The tendon interaction forces, described in [18] in each subsegment j due to the kth tendon is denoted by $\mathbf{F}_{j,k}^{j-1}$, and the resulting moment by $\mathbf{M}_{j,k}^{j-1}$. In addition, there are external and gravitational forces acting on the subsegment with resultant moments. Both these forces must be defined w.r.t. the local frame of reference as

$$\mathbf{F}_g^{j-1} = \left(\mathbf{T}_{j-1}^0\right)^{-1} \begin{bmatrix} 0 & 0 & -m_{disk,j}g & 0 \end{bmatrix}^\top \quad (8)$$

$$\mathbf{F}_{ext}^{j-1} = \left(\mathbf{T}_{j-1}^0\right)^{-1} \mathbf{F}_{ext,j}, \quad (9)$$

where g is the acceleration due to gravity, $\mathbf{F}_{ext,j}$ is the external force applied to disk j, if any, expressed w.r.t. the global frame of reference. The mass of disk j is denoted by $m_{disk,j}$ and includes the additional mass of the locking mechanism, if any. If there is no external force applied to that subsegment, the magnitude of $\mathbf{F}_{ext}$ is set to zero.

Using the equilibrium equations described above and equating them as done in [18], the net force and moment in a subsegment, $\mathbf{F}_j^{j-1}$ and $\mathbf{M}_j^{j-1}$ can be calculated.

Using the constant curvature assumption for each subsegment and Hooke's law, the resulting moment due to bending of the central and passive backbones is given by

$$\mathbf{M}_{elastic}^j = \mathbf{R}(\phi, \theta_j) \begin{bmatrix} 0 \\ E(I_c\kappa_j + \sum_{k=1}^3 I_b\kappa_{j,k}) \\ G(J_c + \sum_{k=1}^3 J_b)\epsilon_j \\ 0 \end{bmatrix} \quad (10)$$

$$\mathbf{R}(\phi, \theta_j) = \mathbf{R}_z(\phi)\mathbf{R}_y(\theta_j) \quad (11)$$

$$\kappa_{j,k} = \frac{\kappa_j}{1 - \kappa_j r_d\cos(\psi_{b,k} - \phi_j)} \quad (12)$$

where I_c, I_b, J_c, and J_b are the second moment of area, and polar second moment of area of the central and passive backbones respectively. Assuming that the central and passive backbones are made of the same material, E and G are the Young's and Shear modulus respectively.

B. Constitutive equations

In addition to the internal moments generated, we assume that each locked portion of the backbones experiences a corresponding internal moment due to the locked state. For a configuration represented by $z_e = (\mathcal{D}_e, \boldsymbol{\tau}_e)$, if the set $\mathcal{D}_e$ consists of d elements, then d unknown internal moments, $\mathbf{M}_{int,i}$, $\forall i = 0, 1, ..d$ are considered to be acting on the subsegments in the locked region.

The function $g(j)$ indicates whether the subsegment j is locked or not.

$$g(j) = \begin{cases} 1 & \text{if locked} \\ 0 & \text{else.} \end{cases} \quad (13)$$

The net internal moment on subsegment j can then be calculated by summing the moments given in (10) and the sum of internal moments resulting from being a part of any of the d locked portions. Transforming the latter to the local frame, the net moment is given by

$$\mathbf{M}_j^{j-1} = \mathbf{M}_{elastic}^j + g(j)\mathbf{T}_j^{j-1}\mathbf{M}_{int,i}^j \quad (14)$$

At equilibrium, the internal moment must be equal to the net moments resulting from force interactions on the robot. Therefore, there are $3n$ equilibrium equations due to moment balance at all n subsegments.

C. Passive backbone length constraints

We can obtain $3d$ additional constraint equations by considering the fixed lengths of the three passive backbones. For any locked portion i between disks p and q, the length of the secondary backbones between them, where $p < q$ can then be calculated using (6) as

$$\ell_k^{p,q} = \sum_{j=p+1}^q \sum_{m=1}^w \left\| \mathbf{p}_{b,(j)}^{j-1}\left(\frac{ml_j}{w}\right) - \mathbf{p}_{b,(j)}^{j-1}\left(\frac{m+1}{w}l_j\right) \right\| \quad (15)$$

where $||.||$ represents the Euclidean norm. For ease of notation, the subscript k is removed from the above equation. If the locked portion between p and q represents the ith locked portion out of d locked portions, $\boldsymbol{\ell}_i$ is the vector representing

the lengths of the passive backbones in it. Once locked, these lengths must remain the same when the robot is bent to another shape by applying a different set of tensions. This constraint can be expressed as

$$\ell_i - \ell_i^* = 0, \forall i = 0, 1, 2, ..d \qquad (16)$$

where ℓ_i^* denotes the backbone lengths of the locked portion predicted by the model after the tendon tensions are changed.

D. Discussion

In the locked state, the system now has $3n + 3d$ equilibrium equations from the moment balance of internal and applied moments. There are also $3n + 3d$ unknown parameters, consisting of the $3n$ curvature parameters as well as the three components of d internal moments generated. When there are no locked portions, the model reduces to that of a general TDCR with $3n$ unknowns and $3n$ constraint equations.

To calculate the final shape at the end of a sequence $\mathcal{Z} = \{z_1, z_2, ...z_T\}$, the model needs to be run successively for each preceeding step. Doing so allows us to 1) calculate the lengths of the locked portions of the passive backbones, and 2) use the curvature values as the model's initial guess to aid convergence when evaluating the next step. The models are computed in MATLAB, using the Trust-region-dogleg algorithm implemented in the *fsolve* function.

V. EXPERIMENTAL VALIDATION

We investigate the performance of our proposed model for different locked configurations of a single segment TDCR. We specifically look at the evaluation of $m = 2$ and $m = 3$ locking mechanisms. The three different case studies considered to evaluate the model and its results are described first. The experimental setup and calibration process are then described, followed by the evaluation.

A. Case studies

Typically, TDCRs with on-board locking mechanisms only consider two mechanisms placed at the base (disk 0) and an intermediate disk. We extend the study to two additional cases as well, considering external tip forces. The robots' final shapes in all three cases are used to evaluate the model.

1) Case 1, (m=2): The locking mechanisms are placed at $\{0, 8\}$. First, disk 0 is locked and the robot is bent using a tension $\boldsymbol{\tau}_1$. Next, the locking mechanism at 8 is locked and another tension $\boldsymbol{\tau}_2$ is applied. The sequence of locking is given by $\mathcal{Z}_1 = \{(\{0\}, \boldsymbol{\tau}_1), (\{0, 8\}, \boldsymbol{\tau}_2)\}$.

2) Case 2, (m=2): Here, locking mechanisms at $\{8, 16\}$ are considered such that the distal portion of the robot is locked. The sequence of locking is given by $\mathcal{Z}_2 = \{(\{16\}, \boldsymbol{\tau}_1), (\{8, 16\}, \boldsymbol{\tau}_2)\}$.

3) Case 3, (m=3): Three locking mechanisms placed at $\{0, 4, 12\}$ are considered. The sequence of locking is given by $\mathcal{Z}_3 = \{(\{0\}, \boldsymbol{\tau}_1), (\{0, 4\}, \boldsymbol{\tau}_2) (\{0, 4, 12\}, \boldsymbol{\tau}_3)\}$.

B. Experimental setup and calibration

To evaluate the three cases in section V-A, two robot prototypes were developed. Both robots are 240 mm long, are actuated by three tendons arranged around the robots' central backbone at angles of $\psi_t = [0, 2\pi/3, 4\pi/3]$, and have three passive backbones placed at angles of $\psi_b = [\pi/3, \pi, 5\pi/3]$. Both the passive backbones and tendons are equidistant from the central backbone, with $r_d = r_{bb} = 4.25\,\text{mm}$. The first robot had locking mechanisms at disks 0, 8, and 16, which could be selectively locked to achieve cases 1 and 2. The second robot had locking mechanisms at disks 0, 4, and 12, and was used for case 3. The locking mechanisms used in these prototypes used set screws for locking. These set screws were manually tightened, engaging them with the robots' passive backbones. While set screw-based locking mechanisms were used in this experiment for simplicity, they can be replaced with any type of locking mechanism, and the model will still be valid. The two robots were actuated by hanging calibrated weights on the tendons.

The desired 2- or 3- curvature robot configurations were achieve by sequentially engaging the robots' locking mechanisms and applying tension to their tendons as discussed in section V-A. The locking sequence for case 3 is shown in Fig. 4. The values of tendon tensions were chosen randomly between 50-450g calibrated weights, with an additional weight of $50\,\text{g}$ used to pretension all the three tendons.

Once the final shape of the robot was achieved (two curvatures in cases 1 and 2, and three curvatures in case 3), a coordinate measurement machine with a point probe (Microscribe G2X, Revware Inc., USA, accuracy of $0.002\,''$) was used to measure the position of every fourth disk on the robot (Fig. 5). Six points were measured around the edge of each fourth disk which were used to find the position of the robot's backbone at that disk. In addition to evaluating the robot in free space, we evaluated the performance of the model for a force acting on the tip at the end of the sequence for cases 1 and 2. Calibrated weights were hung from the end disk using a cable, using a random calibrated weight ranging from $2\,\text{g} - 5\,\text{g}$. Since the configurations are not restricted
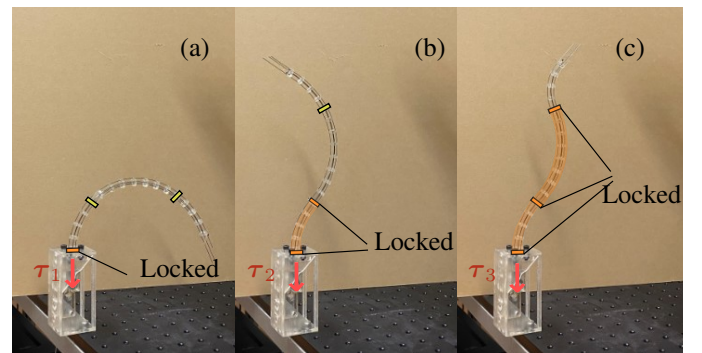
Fig. 4. Locking sequence for a continuum robot with three locking mechanisms placed at 0, 4, 12 for Case 3. (a) The locking mechanism at disk 0 is locked and tension $\boldsymbol{\tau}_1$ is applied. (b) The locking mechanism at disk 4 is locked and tension $\boldsymbol{\tau}_2$ is applied. (c) The locking mechanism at disk 12 is locked and tension $\boldsymbol{\tau}_3$ is applied. The sequence of locking is given by $\mathcal{Z}_3 = \{(\{0\}, \boldsymbol{\tau}_1), (\{0, 4\}, \boldsymbol{\tau}_2) (\{0, 4, 12\}, \boldsymbol{\tau}_3)\}$.
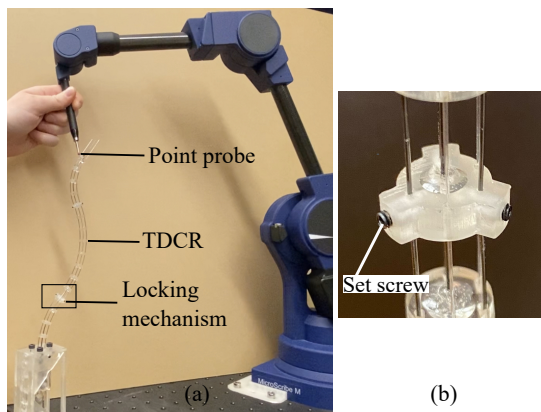
Fig. 5. (a) Experimental setup showing the Microscribe measuring the coordinates of a continuum robot's disks. (b) A zoomed-in image of the locking mechanism, with set screws used for locking

to the planar case, the applied weight results in nonplanar deformations with twists.

For the two prototypes, we use a sample of 25 of the 60 readings to optimise for the Young's modulus of the Nitinol rods as well as the orientation of the base. The latter is expressed as rotation of the experimental data about the global x, y, and z axis. The calibration is posed as a least-squares optimization, minimizing the average Euclidean distance between observed and predicted tip positions. The optimisation was solved using the Nelder-Mead Simplex method, implemented by Matlab's *fminsearch* function.

C. Evaluation of proposed models performance

The model is first evaluated for a TDCR operating in free space. For all three cases, the values of tensions are varied to result in different 3D configurations. A total of 40 configurations are measured and the performance of the model on this dataset is tabulated in Table I. The average end-effector (disk 16) position error is 3.67% ($8.8\,\text{mm}$) w.r.t. total length.

The model was evaluated with an applied tip force over 20 observations presented in Table II. The average position error for the end disk is 3.61% w.r.t. length for the 20 observations ($8.7\,\text{mm}$). The observed errors in the experiments is consistent with the average error of 2.67% observed by Gao et al. [21] for a robot of length $79.2\,\text{mm}$ when modeled with a general friction model for TDCRs. The reported error could be further reduced with a more accurate model of the observed friction, such as that between the passive backbones and disks, but that is currently beyond the scope of this letter. We observe that the errors are higher for case 3 as it has a larger number of actuation steps, with accumulated manual error at each step.

VI. COMPLIANCE ANALYSIS

The effect of the position and number of locking mechanisms on the stiffness of a single segment TDCR is analysed in this section. We assume the effect of gravitational and frictional forces to be negligible in the studies below to study the behaviour of the locking independent of these factors. We consider a robot with 16 disks, with three locking mechanisms. Two of the locking mechanisms are fixed at disks 0 and 16,

whereas the third one is placed on disk d, where the value of d is varied such that $d \in [1, 2, ...15]$.

A. Case Studies

We analyse two configurations achieved through two different sequences of locking :

- **Configuration 1** (proximal portion locked): Locking mechanism at disks $\{0, d\}$ locked with $\mathcal{Z}_1 = \{(\{0\}, \boldsymbol{\tau}_1), (\{0, d\}, \boldsymbol{\tau}_2)\}$.
- **Configuration 2** (distal portion locked): Locking mechanism at disks $\{d, 16\}$ locked with $\mathcal{Z}_2 = \{(\{16\}, \boldsymbol{\tau}_1), (\{d, 16\}, \boldsymbol{\tau}_2)\}$

When the effects of gravity and friction are considered negligible, the shape predicted by the model of the two portions is decoupled. In such a case, a TDCR with n locking mechanisms behaves as an n-segment TDCR. The workspace, forward, and inverse kinematics can be obtained from results already derived for these robots. The more significant difference likely arises from stiffness properties as length constraints imposed by the locking change the inernal stiffness. Therefore, in this section, we study the compliance of the robot using the definition of compliance manipulability index (CMI) in [22].

The CMI is the volume of the compliance manipulability ellipsoid, and is the product of the singular values of the compliance matrix evaluated at the tip of the robot. The compliance matrix itself is evaluated by measuring the change in tip pose per unit wrench applied at the tip. The CMI is always greater or equal to zero. Higher value of CMI indicates a lower stiffness, and a value 0 denotes infinite stiffness.

If we disregard shapes where the entire backbone is locked, there are two major design choices that can be made for the above. One, we can design the system to only be proximally or distally locked (can only achieve configuration 1 or 2). In such a case, only one locking mechanism is required and the backbones can be permanently fixed at either the base or the end disk (as done in multibackbone robot designs [23]).

TABLE I
ERROR STATISTICS FOR DISKS 8 AND 16, EXPRESSED AS % W.R.T LENGTH FOR THE THREE CASES OPERATING IN FREE SPACE FOR ROBOTS OF LENGTH 240 mm.

Disk	Case 1 ($\mathcal{Z}_1$) (15 readings)		Case 2 ($\mathcal{Z}_2$) (15 readings)		Case 3 ($\mathcal{Z}_3$) (10 readings)	
	8	16	8	16	8	16
Average	1.75	3.18	2.45	3.01	2.70	5.38
Median	1.83	2.70	2.32	3.23	2.50	3.63
Minimum	0.45	1.19	0.55	0.98	0.76	1.42
Maximum	2.97	5.96	4.05	6.77	4.26	11.08

TABLE II
ERROR STATISTICS FOR DISKS 8 AND 16, EXPRESSED AS % W.R.T LENGTH FOR CASES 1 AND 2, EXPERIENCING DIFFERENT TIP FORCES OF MAGNITUDE 2 - 5 G FOR ROBOTS OF LENGTH 240 mm.

Disk	Case 1 ($\mathcal{Z}_1$) (10 readings)		Case 2 ($\mathcal{Z}_2$) (10 readings)	
	8	16	8	16
Average	3.00	3.22	1.83	3.99
Median	2.87	2.69	1.79	3.76
Minimum	1.41	1.18	0.54	1.92
Maximum	4.58	6.38	3.60	6.67

Two, the three locking mechanisms can be used as described above, alternating between proximal and distal section being locked (can achieve both configuration 1 and 2). Since the first design choice is a subset of having three locking mechanisms, we study the second design choice in following subsections. First, we propose an actuation strategy in subsection VI-B that can help us leverage the use of three locking mechanisms. Next, we study the variation in robot stiffness or CMI for both configurations in subsection VI-C.

B. Actuating all three locking mechanisms: Strategy to obtain the same robot shape with different compliance

If the secondary backbones are permanently fixed at either the base or the end disk (as done in multibackbone robot designs [23]) but with an additional locking mechanism on an intermediate disk, the robot behaviour can be modeled as that of either Configuration 1 or 2 respectively. Based on the Configuration chosen, the robot will have different stiffness. However, if three locking mechanisms are used (one at the base, one at the end disk, and one along the robot body) instead of permanently fixing the backbones, we can leverage their locking ability to obtain the similar backbone curvatures but with different stiffness as shown in the following subsection.

The actuation strategy is as follows. We observe that when the magnitudes of tendon tension are interchanged in Configuration 2, i.e. $\boldsymbol{\tau}_2$ is first applied, and then $\boldsymbol{\tau}_1$, we obtain the same backbone curvatures. First, the distal section gets locked in a curvature resulting from $\boldsymbol{\tau}_2$, and then the proximal section is bent due to $\boldsymbol{\tau}_1$, resulting in the same shape as configuration 1 as shown in Fig. 6. The two different sequences would be $\mathcal{Z}_1 = \{(\{0\}, \boldsymbol{\tau}_1), (\{0, d\}, \boldsymbol{\tau}_2)\}$ resulting in configuration 1, and $\mathcal{Z}_2 = \{(\{16\}, \boldsymbol{\tau}_2), (\{d, 16\}, \boldsymbol{\tau}_1)\}$, resulting in configuration 2.

This property can be exploited to achieve the same backbone curvatures but with different stiffness properties. The strategy can be extended to more than three locking mechanisms by following the same principle. If the sequence in which tension is applied is reversed, and the disks are locked in decreasing magnitude of their index, starting with the end disk, the same robot shape can be obtained. Theoretically, we could switch between the two configurations with instantaneous changes in tendon tensions and locked states of the disks. However, as mechanical components cannot be instantaneously actuated, vibration and robot motion are to be expected.

C. Actuating two locking mechanisms: Variation in robot compliance

This subsection studies the variation in robot compliance when proximally or distally locked with varying values of the location d of the third locking mechanism. First, the robot is bent to a C-shape and then the locking mechanism at disk d is locked resulting in either the proximal or the distal portion being locked. Without changing the tendon tension, the robot compliance is calculated. The value of tendon tension is approximated as $\boldsymbol{\tau}_1 = \boldsymbol{\tau}_2 = [\tau, 0, 0]$ where $\tau = \frac{\pi}{2lr_d}E(I_c + 3I_b)$ to estimate the tension required to achieve 90 degree bending of the robot. This value is calculated using the Euler-Bernoulli
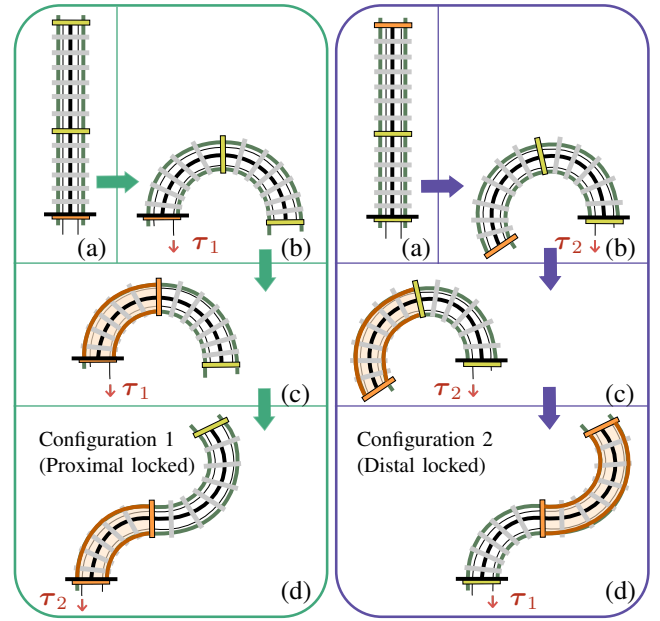

Fig. 6. Strategy to obtain the same backbone curvature through two different locking sequences, with Configuration 1 (proximal section locked) in green boxes and Configuration 2 (distal section locked) in purple boxes. From the straight configuration in (a), the robot is bent by applying a tendon tension of $\boldsymbol{\tau}_1$ for 1 and $\boldsymbol{\tau}_2$ for 2, shape (b) is obtained. Once the proximal and distal section is locked in (c), by applying antagonistic tendon tension, shape (d) is obtained, with the same backbone curvatures in both sections.
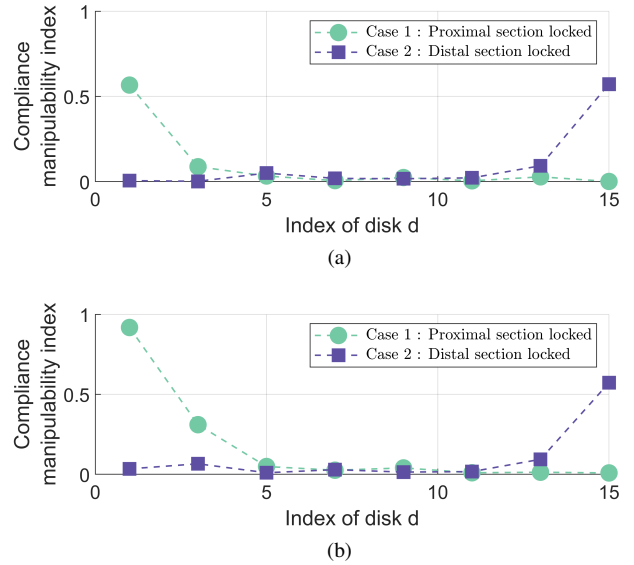

Fig. 7. Variation of compliance manipulability index for when the robot is bent to (a) a C-shape and (b) an S-shape.

beam theory by assuming that the effective flexural rigidity of the primary and secondary backbones is given by $E(I_c + 3I_b)$. The variation of CMI with the index of the locked disk, d is plotted in Fig. 7 (a). The overall compliance in both cases reduces compared to a single segment TDCR with no locked portion, which has a CMI of 1.36 when bent to a C-shape. Therefore, we see that the robot is more compliant in the absence of locking mechanisms.

Next, we study the variation of stiffness when the robot is bent to an S-shape. We apply the strategy described in the

subsection VI-C, where the values of $\boldsymbol{\tau}_1$ and $\boldsymbol{\tau}_2$ are interchanged to achieve the same configuration. For configuration 1 (proximally locked), the value of $\boldsymbol{\tau}_1 = [\tau, 0, 0]$ is retained, and $\boldsymbol{\tau}_2 = 2[0, \tau, \tau]$ to ensure that the S-shaped curve is formed. The values are interchanged for configuration 2. The observed CMI are plotted in Fig. 7(b).

We observe that the difference in compliance between proximal and distal portions being locked is not significant when the length of the locked portion lies approximately between $30 - 70\%$. As the length of the locked portion decreases, the length of the deforming unlocked portion increases, resulting in a more compliant robot. The compliance reduces sharply when the length of the locked portion greater than approximately $20 - 25\%$ of the entire length. Comparing the robot compliance between S-shape and C-shape configurations for given locking disk index, the largest differences are observed for Case 1 when the index is below 5. This difference is because the length of the locked portion is smaller than the free moving portion, which then bends to form an S-shape that differs widely from the corresponding C-shape. The compliance otherwise doesn't vary significantly because the resulting shape is similar in both cases to a C-shape. All the above could inform the placement of the locking mechanism based on the stiffness requirements as well as advise design choices when implementing the strategy proposed in subsection VI-B.

VII. Conclusion and future work

In this work we proposed a static model for a TDCR with locking mechanisms that can account for variation in curvature along the backbone while considering frictional and gravitational forces. The backbone curvature representation includes twist, which allows for the modeling of 3D deformations. In addition, we demonstrate that locking can be used to modulate the robot stiffness without changing its shape using an appropriate actuation strategy. The design analysis highlights the variation of robot compliance with placement of locking mechanisms. Based on the task's compliance requirements, the location and number of locking mechanisms can be determined. While we assume that the passive backbones run parallel to the central backbone and do not experience friction at disks, the modeling can be further improved by accounting for their buckling and frictional forces. In the current work, we analyse the performance of the robot for up to three locking mechanisms. Future work will benefit from analysing the design choices and consequences of adding additional mechanisms on the robot properties. The proposed strategy to achieve different stiffness can inform their motion planning and will be investigated in future work.

References

[1] M. Cianchetti, T. Ranzani, G. Gerboni, T. Nanayakkara, K. Althoefer, P. Dasgupta, and A. Menciassi, "Soft robotics technologies to address shortcomings in today's minimally invasive surgery: The stiff-flop approach," *Soft Robotics*, vol. 1, no. 2, pp. 122–131, 2014.

[2] S. M. H. Sadati, Y. Noh, S. Elnaz Naghibi, K. Althoefer, and T. Nanayakkara, "Stiffness control of soft robotic manipulator for minimally invasive surgery (mis) using scale jamming," in *Intelligent Robotics and Applications*, H. Liu, N. Kubota, X. Zhu, and R. Dillmann, Eds. Springer International Publishing, 2015, pp. 141–151.

[3] Y.-J. Kim, S. Cheng, S. Kim, and K. Iagnemma, "Design of a tubular snake-like manipulator with stiffening capability by layer jamming," in *2012 IEEE/RSJ International Conference on Intelligent Robots and Systems*, 2012, pp. 4251–4256.

[4] M. Langer, E. Amanov, and J. Burgner-Kahrs, "Stiffening sheaths for continuum robots," *Soft Robotics*, vol. 5, no. 3, pp. 291–303, 2018.

[5] Y.-J. Kim, S. Cheng, S. Kim, and K. Iagnemma, "A stiffness-adjustable hyperredundant manipulator using a variable neutral-line mechanism for minimally invasive surgery," *IEEE Transactions on Robotics*, vol. 30, pp. 382–395, 2014.

[6] A. Stilli, H. A. Wurdemann, and K. Althoefer, "Shrinkable, stiffness-controllable soft manipulator based on a bio-inspired antagonistic actuation principle," in *IEEE/RSJ International Conference on Intelligent Robots and Systems*, 2014, pp. 2476–2481.

[7] B. Zhao, L. Zeng, Z. Wu, and K. Xu, "A continuum manipulator for continuously variable stiffness and its stiffness control formulation," *Mechanism and Machine Theory*, vol. 149, p. 103746, 2020.

[8] J. Starke, E. Amanov, M. T. Chikhaoui, and J. Burgner-Kahrs, "On the merits of helical tendon routing in continuum robots," in *IEEE International Conference on Intelligent Robots and Systems*, 2017, pp. 6470–6476.

[9] A. Gao, H. Liu, Y. Zhou, Z. Yang, Z. Wang, and H. Li, "A cross-helical tendons actuated dexterous continuum manipulator," in *IEEE International Conference on Intelligent Robots and Systems*, 2015, pp. 2012–2017.

[10] K. Oliver-Butler, J. Till, and C. Rucker, "Continuum Robot Stiffness under External Loads and Prescribed Tendon Displacements," *IEEE Transactions on Robotics*, vol. 35, no. 2, pp. 403–419, 2019.

[11] S. Wang, R. Zhang, D. A. Haggerty, N. D. Naclerio, and E. W. Hawkes, "A Dexterous Tip-extending Robot with Variable-length Shape-locking," *IEEE International Conference on Robotics and Automation*, pp. 9035–9041, 2020.

[12] C. Yang, S. Geng, I. Walker, D. T. Branson, J. Liu, J. S. Dai, and R. Kang, "Geometric constraint-based modeling and analysis of a novel continuum robot with Shape Memory Alloy initiated variable stiffness," *The International Journal of Robotics Research*, vol. 39, no. 14, pp. 1620–1634, 2020.

[13] C. Bishop, M. Russo, X. Dong, and D. Axinte, "A Novel Underactuated Continuum Robot With Shape Memory Alloy Clutches," *IEEE/ASME Transactions on Mechatronics*, 2022.

[14] C. Pogue, P. Rao, Q. Peyron, J. Kim, J. Burgner-Kahrs, and E. Diller, "Multiple curvatures in a tendon-driven continuum robot using a novel magnetic locking mechanism," in *IEEE/RSJ International Conference on Intelligent Robots and Systems*, 2022, pp. 472–479.

[15] B. Kang, R. Kojcev, and E. Sinibaldi, "The First Interlaced Continuum Robot, Devised to Intrinsically Follow the Leader," *PLOS ONE*, vol. 11, 2016.

[16] P. Wang, S. Guo, F. Zhao, X. Wang, and M. Song, "Follow-the-leader deployment of the interlaced continuum robot based on the unpowered lock mechanism," in *Intelligent Robotics and Applications. Lecture Notes in Computer Science*, vol. 13015, 2021, pp. 448–459.

[17] L. Wang, G. Del Giudice, and N. Simaan, "Simplified Kinematics of Continuum Robot Equilibrium Modulation via Moment Coupling Effects and Model Calibration," *Journal of Mechanisms and Robotics*, vol. 11, no. 5, 2019.

[18] P. Rao, Q. Peyron, S. Lilge, and J. Burgner-Kahrs, "How to Model Tendon-Driven Continuum Robots and Benchmark Modelling Performance," *Frontiers in Robotics and AI*, vol. 7, p. 223, 2021.

[19] W. S. Rone and P. Ben-Tzvi, "Mechanics modeling of multisegment rod-driven continuum robots," *Journal of Mechanisms and Robotics*, vol. 6, no. 4, 2014.

[20] H. Yuan, L. Zhou, and W. Xu, "A comprehensive static model of cable-driven multi-section continuum robots considering friction effect," *Mechanism and Machine Theory*, vol. 135, pp. 130–149, 2019.

[21] A. Gao, Y. Zou, Z. Wang, and H. Liu, "A general friction model of discrete interactions for tendon actuated dexterous manipulators," *Journal of Mechanisms and Robotics*, vol. 9, no. 4, 2017.

[22] M. Khadem, L. Da Cruz, and C. Bergeles, "Force/Velocity Manipulability Analysis for 3D Continuum Robots," in *IEEE International Conference on Intelligent Robots and Systems*, 2018, pp. 4920–4926.

[23] N. Simaan, K. Xu, A. Kapoor, W. Wei, P. Kazanzides, P. Flint, and R. Taylor, "Design and integration of a telerobotic system for minimally invasive surgery of the throat," *The International journal of robotics research*, vol. 28, pp. 1134–1153, 09 2009.